Observation of magnetic field-induced second magnetic ordering and peculiar ferroelectric polarization in L-type ferrimagnetic $Fe_2(MoO_4)_3$

Ajay Tiwari [1], D. Chandrasekhar Kakarla,[1,*] M.-J. Hsieh,[2] J.-Y Lin,[2,3] C. W. Wang [4], L. K. Tseng [1], C. E. Lu,[1]
Arkadeb Pal,[1] T. W. Kuo,[1] Mitch M. C. Chou,[5,6] and H. D. Yang [1,6,†]

[1]*Department of Physics, National Sun Yat-sen University, Kaohsiung 80424, Taiwan*
[2]*Institute of Physics, National Yang Ming Chiao Tung University, Hsinchu 30010, Taiwan*
[3]*Center for Emergent Functional Matter Science, National Yang Ming Chiao Tung University, Hsinchu 30010, Taiwan*
[4]*National Synchrotron Radiation Research Center, Hsinchu 30076, Taiwan*
[5]*Department of Materials and Optoelectronic Science, National Sun Yat-sen University, Kaohsiung 80424, Taiwan*
[6]*Center of Crystal Research, National Sun Yat-sen University, Kaohsiung 80424, Taiwan*

$Fe_2(MoO_4)_3$ was synthesized and characterized as a prototype of L-type ferrimagnets (L-FiM) with an ordering temperature $T_{N1} \sim 12$ K using magnetic susceptibility (χ), specific heat (C_p), and dielectric (ε') anomaly. Two remarkable findings are magnetic field (H) induced (i) an additional magnetic phase transition at T_{N2} below T_{N1}; and (ii) the emergence of flexible ferroelectric polarization (P) with the tuning parameters H and T below T_{N2}. Thus, the H-T phase diagram for spin-induced type-II multiferroics was established. In contrast to some known multiferroics with a critical field-induced spin-flip P below T_{N1}, the observed multiferroic nature is exotic. The origin of the profound multiferroic nature may be hidden in the complex T-and H-dependent spin and lattice structures. Consequently, the schematic picture of H-induced possible change of lattice symmetry and conical spin structure has been proposed. More experimental and theoretical works providing solid evidence and interpretations have been suggested to explore these peculiar multiferroic phenomena.

I. INTRODUCTION

Type-II multiferroics with strong cross coupling enable the electric field control of magnetism (and vice versa) and are anticipated to widen the bottleneck of state-of-the-art spintronic technology [1]. Although conventional materials exclude the coexistence of magnetic and electric polarization (P), recent progress has explored unconventional ways to combine them in both collinear and noncollinear spin geometries, which can be explained by various spin-induced microscopic mechanisms [2–9]. In magnetic ferroelectrics, the spatial inversion symmetry is broken by the peculiar arrangement of spins resulting in finite P [4,7]. The deep roots of connectivity between magnetic and electric entities occur via either one or more of the microscopic glues: (i) spin-orbital, (ii) spin-lattice, and (iii) spin-charge couplings [8]. Noncollinear spin-spiral states or collinear spin ↓↓↑↑ configurations dominate type-II multiferroic research [4,10–12]. Furthermore, the polar crystal lattice enhances P in multiferroic systems [9]. Competing factors, such as low-dimensional magnetism, peculiar spin-frustrated lattices, complex magnetic exchange interactions, and magnetic/crystalline anisotropy energies, determine the formation of either collinear or noncollinear spin structures [4,7,8]. Additionally, in many multiferroics sys-

tems, critical fields evoke a spin-flip transition that manifests the enhancement of P [3,4,11–17].

$A_2(MO_4)_3$ (A = trivalent cation and M = Mo and W) materials have received tremendous attention owing to their flexible crystal structure, which provides distinctive catalyst and thermal expansion properties [18]. More specifically, magnetic molybdates (A = RE or TM ions) are of particular interest because of their unique ferroelastic and ferroelectric properties [19]. Unlike conventional ferroelectrics, rare-earth-based molybdates belong to a class of displacive ferroelectrics without a soft polar mode [20,21]. This improper spontaneous P emerges from an elastic instability that gives rise to spontaneous strain in the original piezoelectric paraelectric phase [20]. Recently, T-dependent x-ray diffraction (XRD) has established that improper spontaneous P arises from structural instability, which leads to the displacement of different cations with distinct critical behavior [22]. Further, magnetic field (H) induced large linear magnetoelectric (ME) phenomena owing to magnetic crystalline anisotropy have been established in these systems [23]. In contrast to rare-earth molybdates, less attention has been paid to exploring the magnetic and ME properties of transition-metal-ion-based molybdates. Structural reports are available on two known $Fe_2(MoO_4)_3$ and $Cr_2(MoO_4)_3$ systems; an orthorhombic to monoclinic transformation with a ferroelastic nature was established at high temperature [19,24,25]. Reports on the single crystal x-ray diffraction were indexed with two distinct space groups, $P2_1/a$ (centrosymmetric nonpolar with four distinct Fe sites) and $P2_1$ (noncentrosymmetric polar with eight

*Corresponding author: chandu@mail.nsysu.edu.tw
†Corresponding author: yang@mail.nsysu.edu.tw

distinct Fe sites) [26]. Despite two space groups being different, the chemical environment of Fe^{3+} is similar, where the corner shared FeO_6 octahedra was connected MoO_4 tetrahedral three dimensionally. However, centrosymmetric $P2_1/a$ was widely accepted in the literature based on the grounds of the absence of a second harmonic signal in $Fe_2(MoO_4)_3$ single crystals [24]. $Fe_2(MoO_4)_3$ is a prototype example of an L-type ferrimagnet (L-FiM) with long-range magnetic ordering at $T_{N1} \sim 12$ K [27,28]. Combined low-temperature Mössbauer and susceptibility results were used to enlighten the L-type ferrimagnetic structure for $Fe_2(MoO_4)_3$ [27]. The Mössbauer effect spectra reveal ferrimagnetic behavior despite having a similar oxidation state (Fe^{3+}) and chemical environment (FeO_6) [27]. Below T_{N1}, the temperature-dependent sublattice magnetizations saturate at slightly different rates owing to the minor variations in the magnetic exchange paths between Fe ions [29]. This generates a difference in the magnetic hyperfine field of the four iron sites and leads to weak ferrimagnetic behavior. However, as $T \to 0$ K, the hyperfine fields trend to saturated at similar values resulting in nearly perfect antiferromagnetic ordering [27,29]. Moreover, the magnetic interaction between two Fe^{3+} ions occurred via complicated $Fe^{3+}-O^{2-}-Mo^{6+}-O^{2-}-Fe^{3+}$ supersuperexchange paths [27–30]. These motivated us to explore the magnetic and ME properties of $Fe_2(MoO_4)_3$ further in the magnetic fields.

II. EXPERIMENTAL DETAILS

Polycrystalline $Fe_2(MoO_4)_3$ was synthesized using the conventional solid-state method previously prescribed in Ref. [31]. The phase purity of the $Fe_2(MoO_4)_3$ was ascertained using high-resolution synchrotron x-ray diffraction (SXRD) with the 19A beamline of the Taiwan Photon Source at the National Synchrotron Radiation Research Center (NSRRC), Taiwan. For SXRD, the polycrystalline $Fe_2(MoO_4)_4$ fine powder was loaded in a glass capillary of 0.3 mm diameter. The data were collected using the reflection geometry with a wavelength of $\lambda = 0.61992$ Å and a double crystal monochromator Si (111) with an energy resolution of 1.33×10^{-4}. Diffraction data were collected in the 2–120° range in steps of 0.004°. Rietveld refinement of the SXRD data was performed using FULLPROF suite software. The surface morphology was examined by scanning electron microscope (SEM, FEI Quanta-200) equipped with an energy dispersive x-ray spectrometer (EDS) analyzer. Figure S1(a) of the Supplemental Material shows an SEM micrograph that demonstrates random shaped grains (size distribution of 10–50 μm) separated by grain boundaries [32]. The quantitative analysis by EDS revealed that a Fe:Mo:O ratio of 0.129:0.179:0.692 is close to the expected stoichiometry of $Fe_2(MoO_4)_3$. DC magnetic measurements under fields were carried out in the Quantum Design magnetic property measurement system (MPMS-XL7). Magnetic measurements were performed in zero field cooling (ZFC) and field cooling (FC) protocols on a finely grounded powder sample. The specific heat $C_p(T, H)$ was measured with a heat-pulsed thermal relaxation calorimeter in the physical property measurement system (PPMS). A precision Agilent 4294A LCR meter with an operating voltage of $V_{AC} = 10$ V was used for T- and

H-dependent dielectric measurements. Pyroelectric current (I_{py}) measurements were made with a Keithley 6517B electrometer. Silver paste has been applied on both sides of the sample ($a \sim 12$ mm² and $d \sim 0.2$ mm) to make parallel plate geometry for dielectric and I_{py} measurements. Dielectric and I_{py} measurements were performed in MPMS-XL7 with the user-designed probe. For I_{py} measurement, ME poling was applied at 35 K (far above T_{N1} with $H = 7$ T and electric field $E = \pm 2.6$ kV/cm) and subsequentially cool to the lowest $T = 2$ K and removed the stray charges by short circuiting the leads for about 20 min at 2 K. I_{py} was recorded while heating under the same H and zero electric fields. The P was calculated by integrating the time dependence of the $I_{py} = \int \frac{i}{a} \partial t$; where a and t denote area and time respectively. All the pyrocurrent and dielectric measurements were performed in $H \perp E$ geometry.

III. RESULTS

A. Crystal structure

The high-resolution SXRD pattern of $Fe_2(MoO_4)_3$ was analyzed using the $P2_1/a$ space group through Rietveld refinement, as shown in Fig. 1(a), and the corresponding fitting parameters are summarized in Table S1 of the Supplemental Material [32]. The crystal structure contains four distinct Fe sites, which form the three-dimensional framework of the FeO_6 octahedra by corner sharing with the neighboring MoO_4 tetrahedra [Figs. 1(b) and 1(c)]. The average bond lengths ($\langle Fe-O \rangle$) of the four Fe sites indicate two Fe sites (Fe2 and Fe3) among the four experienced similar crystal-field environments (shown in Table S2 [32]). Fe2O_6 and Fe3O_6 are highly distorted with the shortest $\langle Fe-O \rangle$ bond lengths and a bond angle that generates different crystal fields for Fe2 and Fe3 magnetic ions.

B. Magnetic, thermal, and electric properties

$Fe_2(MoO_4)_3$ is a well established L-type ferrimagnet. Despite having a similar valence state (Fe^{3+}) and chemical environment (FeO_6) for all four Fe sites, a weak FiM component resulted from the incomplete compensation of the collinear arrangement of Fe^{3+} ions aroused by the difference in $\langle Fe-Fe \rangle$ bond lengths and $\langle Fe-O-Mo \rangle$ bond angles [29]. To further confirm the L-type FiM of $Fe_2(MoO_4)_3$, a low field magnetization has been presented in Fig. S2 [32] and Fig. 2(a). The χ vs T nature of ZFC and FC curves at $H = 0.1$ T represent the typical L-FiM behavior with an almost zero value of χ at the paramagnetic (PM) region. A long-range ordering is established at $T_{N1} \sim 12$ K; with a further decrease in T, χ decreases monotonically and approaches zero as $T \to 0$. Overall, $\chi(T)$ is similar to that of the L-FiM ordering [28]. The specific heat (C_p) at $H = 0$ T with cooling and heating curves [Fig. 2(b)] exhibits a characteristic λ-shaped anomaly at $T_{N1} \sim 12$ K, without the thermal hysteresis manifesting a second-order phase transition with long-range magnetic order. In addition, ε' vs T cooling and warming curves [Fig. 2(c)] at 0 T exhibits a slope change at T_{N1} followed by a rapid decrease below T_{N1}. The coincidence of magnetic, thermal, and dielectric anomalies indicates a strong correlation among the magnetism, thermodynamics,
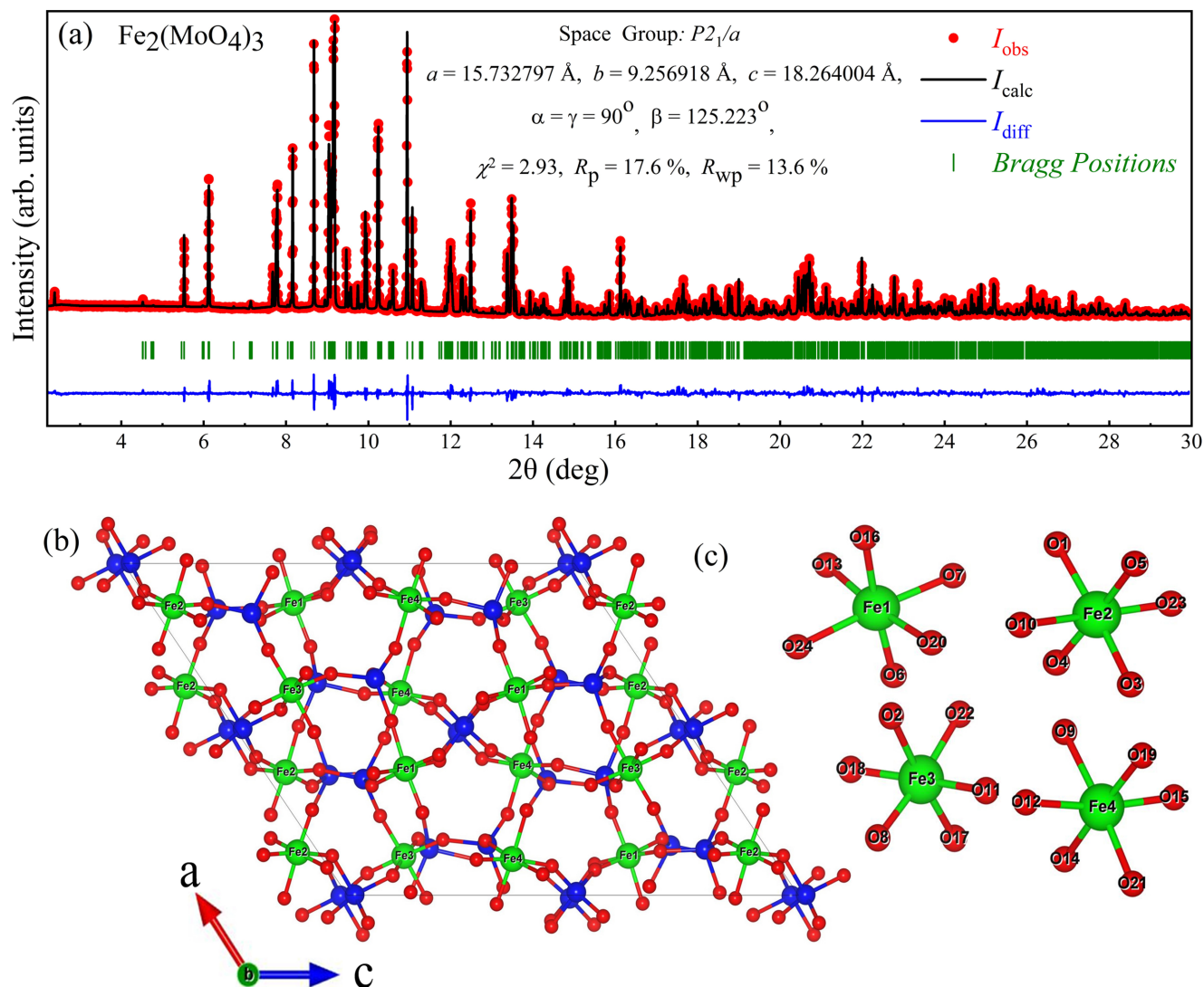
FIG. 1. (a) Experimental SXRD pattern with the Rietveld refinement of $Fe_2(MoO_4)_3$ at 300 K. (b) Crystal structure of $Fe_2(MoO_4)_3$, where the FeO_6 octahedra corner is connected with the MoO_4 (Mo atoms are in blue) tetrahedra, which enables supersuperexchange interactions through the Fe-O-Mo-O-Fe path. (c) Fe-O bond lengths of all four distorted FeO_6 (tabulated in Table S2).

and electric properties of this system at $H = 0$ T. A similar trend of ε' vs T curves was observed in several multiferroic systems, which was ascribed to the lattice ε' anomaly [33–35].

The $\chi(T)$ vs T at different H values was presented in Fig. 2(d). H strongly affects the overall $\chi(T)$ profile. The magnetic anomaly at T_{N1} was progressively suppressed and became broader and smeared for H up to 7 T, whereas T_{N1} was maintained unchanged. More remarkably, H induced an additional magnetic anomaly upturn at T_{N2} below T_{N1}. It is noted that the anomaly at T_{N2} was continuously enhanced and shifted toward T_{N1} with increasing H. An apparent saturated trend of the $\chi(T)$ curve at low T suggests the more ferromagnetic (FM)-like nature of this transition. Further absence of irreversibility between ZFC-FC curves at 7 T suggests T_{N2} belongs to the second-order magnetic transition (Fig. S3 [32]). To gain further insight into the magnetic anomaly at T_{N2}, $C_p/T(T)$ in H up to 9 T is depicted in Fig. 2(e) which demonstrates a clear and startling trend. An H-induced anomaly

emerges at T_{N2}, consistent with the anomaly in $\chi(T, H)$ data. It is plausible that the emerging anomaly of $\chi(T, H)$ corresponds to the simple phase transition as observed in C_p/T. Simultaneously, the original transition anomaly at T_{N1} was gradually suppressed with increasing H. $C_p/T(T)$ at $H = 9$ T is particularly intriguing. The results show that a robust long-range order is established at T_{N2} under applying H. These results imply that, in even higher H, there might exist only one phase transition at T_{N2} at the expense of the T_{N1} phase. Following these unique $\chi(T, H)$ and $C_p/T(T, H)$ data, the $\varepsilon'(T, H)$ curves shown in Fig. 2(f) demonstrate an exotic dielectric response, where the application of H induces a second ε' anomaly at T_{N2}, below T_{N1}, and it progressively shifts to higher T with increasing H. Amusingly, the onset of T_{N2} matched the second transition in the $\chi(T, H)$ and $C_p/T(T, H)$ curves. This suggests a complicated coupling between the magnetic, thermal, and electric properties of the system at T_{N2}. This coupling might be distinct from that at T_{N1}.
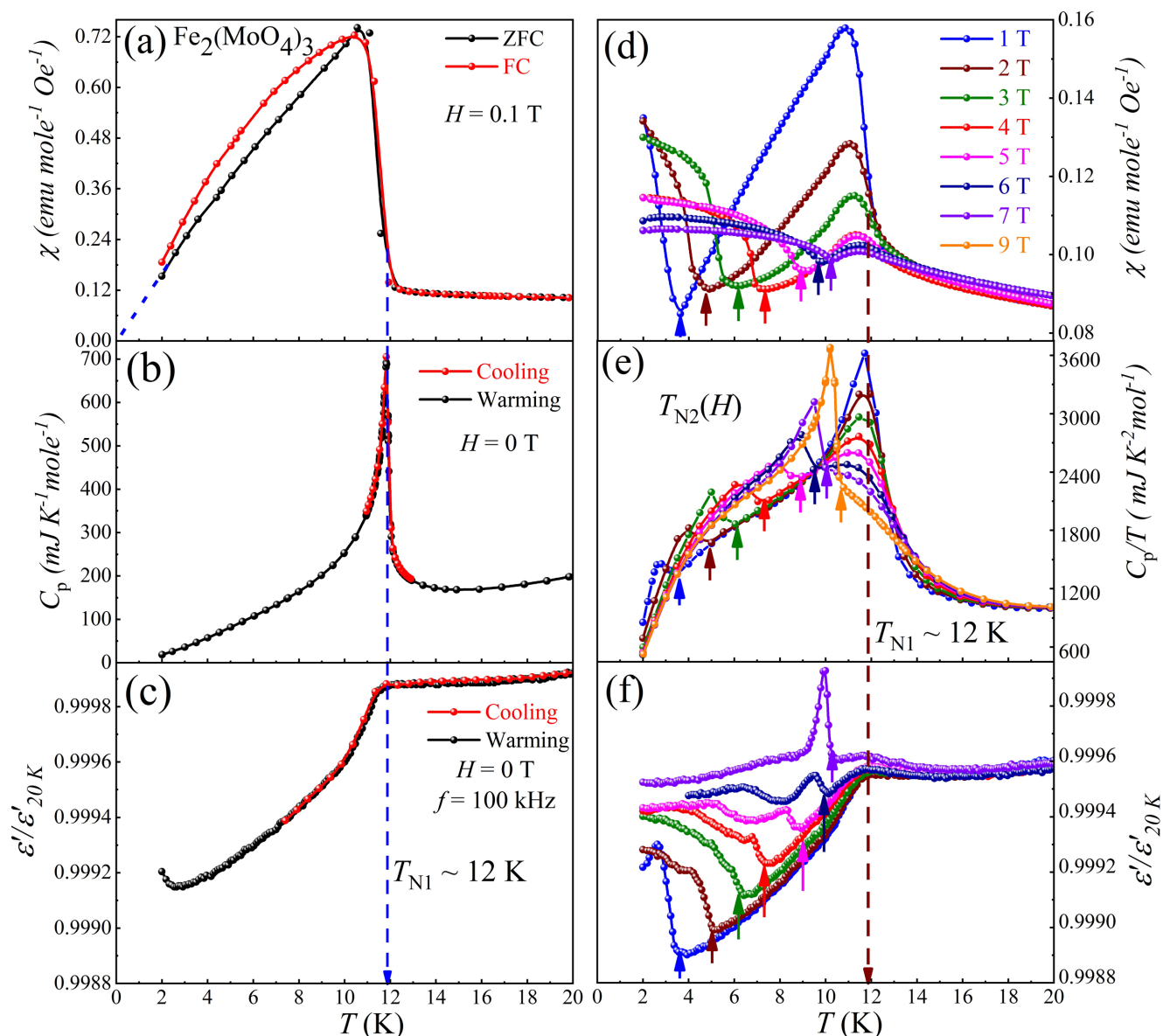
FIG. 2. χ, C_p, and ε' for $T = 2$ to 20 K. (a) χ vs T (ZFC-FC) curves at $H = 0.1$ T; (b) C_p vs T at $H = 0$ T; (c) ε' vs T at $H = 0$ T and frequencies $(f) = 100$ kHz; (d) χ vs T, (e) C_p/T vs T, and (f) ε' vs T under $H = 1–7$ T with $\Delta H = 1$ T. The color arrows in (d)–(f) illustrate the onset of T_{N2} for the respective H values in the χ, C_p/T, and ε' curves.

C. Magnetoelectric properties

To elucidate the ferroelectric nature of $Fe_2(MoO_4)_3$ at T_{N1} and T_{N2}, H-dependent I_{py} vs T curves along with the corresponding P values were measured [shown in Figs. 3(a) and 3(b)]. For $H = 0$, within the resolution limit of the experimental setup, I_{py} is almost zero over the entire measured T window. This result is consistent with ε' vs T for $H = 0$, suggesting that the lattice dielectric anomaly does not lead to P at T_{N1}. A sharp peak in I_{py} at the onset of T_{N2} for $H = 7$ T confirms that T_{N2} is responsible for P. Further, the switching of P by changing the poling direction of the electric field (E) at $H = -7$ T confirms the ferroelectric nature of the transition at T_{N2}. Notably, I_{py} remains zero at T_{N1}, even for $H = 7$ T, which excludes the existence of spin-induced ferroelectricity near T_{N1}. To verify and correlate the continuous variations in T_{N2} with the H, the I_{py} vs T curves are shown at

different H in Fig. 3(c). A minute broad peak in $I_{py}(\sim 0.5$ pA) starts to appear even for a low $H(= 1$ T) value at $T_{N2} = 3$ K. When H increases, I_{py} becomes more pronounced, sharper, and enhanced in magnitude up to $I_{py} = 3.9$ pA for $H = 7$ T. In Fig. 3(d), $P = 0$ over the entire T range as $H = 0$. However, P can be observed for $H \neq 0$, even at relatively low H values. For $H = 1$ T, P increased sharply below T_{N2} and became saturated at low T. As H increased above 1 T, T_{N2} shifted to a higher T, and P saturates at 2.8×10^{-4} $(\mu C/cm^2)$ below $T = 2$ K. A DC bias pyrocurrent (I_{DC}) measurement was performed to check the intrinsic ferroelectric ordering. Unlike conventional I_{py} measurement, in the DC bias technique, the electric field remained switched on and I_{py} was collected during the warming of the sample. The DC bias acts as a poling field below ferroelectric transition, polarizing the dipoles. Thus, for intrinsic ferroelectric transition, DC bias
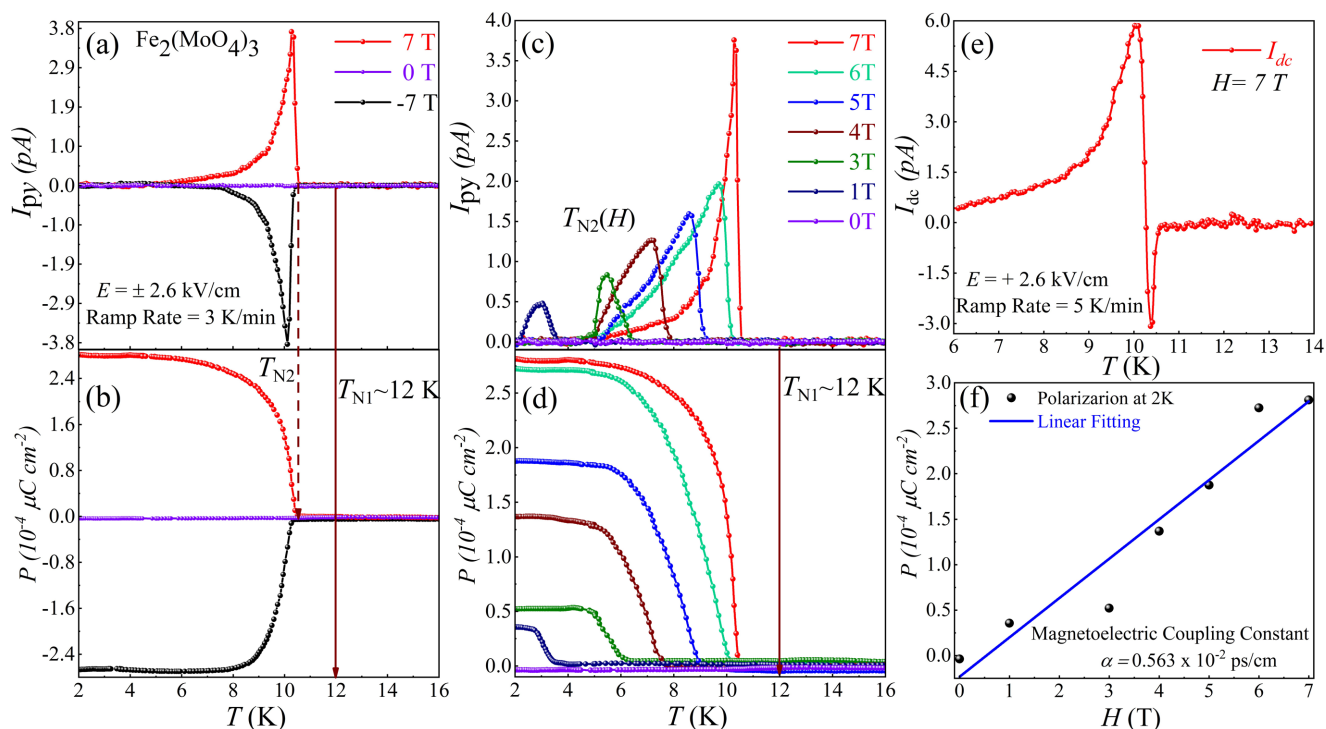
FIG. 3. (a) I_{py} and (b) P of $Fe_2(MoO_4)_3$ under $H = 0$ and ± 7 T with a pooling electric field of ± 2.6 kV/cm; (c) I_{py} (H, T); (d) P (H, T), which follow χ vs T, C_p/T vs T, and ε' vs T as shown in Fig. 2; (e) I_{py} under DC bias at $H = 7$ T with a pooling electric field of $+2.6$ kV and a ramp rate of 5 K/min, showing intrinsic ferroelectric behavior; (f) P vs H curve at $T = 2$ K; the solid blue line represents the linear fit to estimate the magnetoelectric coupling coefficient.

results in two I_{py} peaks: one upward peak due to the P of the ferroelectric dipoles and then a downward peak due to the depolarization of these polarized dipoles across the transition. However, such a typical feature is not observed in extrinsic cases such as leakage currents or thermally stimulated free charge carriers. The two peaks in the DC bias pyrocurrent (I_{DC}) data [shown in Fig. 3(e)] confirm the true nature of the ferroelectric ordering at T_{N2}. The linear ME coupling constant $\alpha = 0.563 \times 10^{-2}$ ps/cm shown in Fig. 3(f) is of comparable order to that of known linear ME materials, such as Cr_2O_3 and Co_4Nb_2O [36–38].

D. *H-T* phase diagram

With the systematic data of $\chi(T, H)$, C_p/T (T, H), ε' (T, H), and P (T, H), the multiferroic phase diagram of $Fe_2(MoO_4)_3$ shown in Fig. 4 can be delineated with the corresponding anomalies in Figs. 2 and 3. For $H = 0$, with decreasing T, $Fe_2(MoO_4)_3$ changes from the PM state at high T to an L-FiM state below T_{N1}. With a finite value of $H = 0.35$ T, one more phase boundary below T_{N2} develops with the new anomaly in χ in the (T, H), C_p/T (T, H), ε' (T, H), and P (T, H) data at T_{N2}. This phase boundary continuously shifts toward higher T and approaches T_{N1} with increasing H. Curiously, P begins to develop below the phase boundary, indicating that L-FiM changes into another magnetic ordering phase under H where the polarization appears and is known as the multiferroic region. These results demonstrated that $Fe_2(MoO_4)_3$ belongs to the type-II multiferroic state below T_{N2}. In type-II multiferroics, the origin of P is closely

associated with specific spin configurations. Detailed knowledge of the spin structure is a prerequisite for understanding
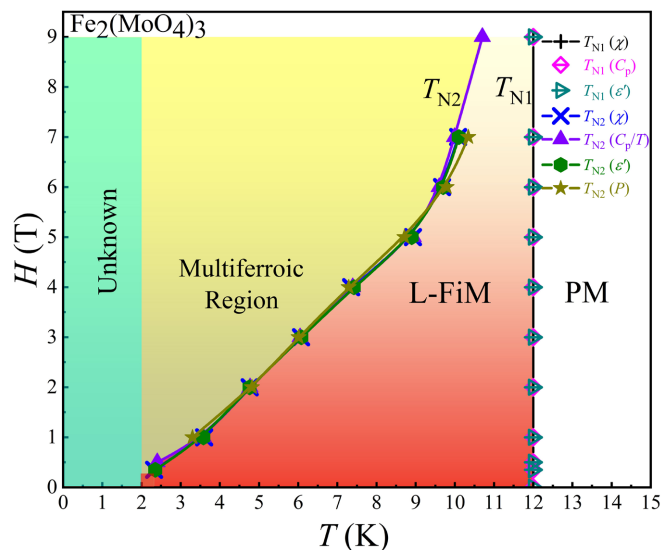

FIG. 4. *H-T* multiferroic phase diagram of $Fe_2(MoO_4)_3$ determined by χ vs T, C_p/T vs T, and ε' vs T (Figs. 1 and 2). The vertical black line at $T_{N1} \sim 12$ K indicates the transition from a PM to an L-FiM ordering state. The second phase boundary of T_{N2} from L-FiM and multiferroic region where the polarization appears is highly sensitive to the applied H. The white, red, yellow, and cyan areas indicate the PM, L-FiM, multiferroic region, and unknown area (owing to the limitation of the experimental window), respectively.

the spin-charge coupling mechanism in type-II multiferroics [4]. Unfortunately, no reports are available on the spin structure of $Fe_2(MoO_4)_3$ under H. Although a reasonable L-FiM spin structure has been proposed from neutron powder experiments at $H = 0$, the ground-state magnetic structure has not yet been fully resolved and remains an open question. Although the H-T phase diagram established a peculiar type-II multiferroic $Fe_2(MoO_4)_3$, several questions remain unanswered. (i) Why is electric P absent for L-FiM order below T_{N1}? (ii) Why does P only emanate below T_{N2}? (iii) Why is T_{N2} strongly modulated by external H? The possible answers to these questions might lie in the crystal and spin structures, along with complicated magnetic supersuperexchange paths.

IV. DISCUSSION AND PROPOSED MECHANISM

$Fe_2(MoO_4)_3$ has a complex crystal structure with four different iron crystallographic sites in a three-dimensional lattice. Each iron atom is surrounded by six (MoO_4) tetrahedra that prevent the direct Fe-O-Fe superexchange interaction; indeed, supersuperexchange interactions have been reported via Fe-O-Mo-O-Fe [30]. Each iron atom has eight nearest neighbors and six next-nearest neighbors that provide 14 distinct exchange links (Fe-O-Mo-O-Fe) [30]. The net orientation of the spins was controlled by the strength of the exchange interactions between the sites. The supersuperexchange interactions were determined by the semiempirical rule, with the assumption of a dominant AFM interaction, where the strength increases with the decrease of bond length and increase of bond angles [30]. The pair of magnetic moments, Fe1-Fe3 to Fe2-Fe4, aligns antiferromagnetically with an incomplete compensation of the collinear arrangement. This assignment justifies the finite FM moment at low T and the reasonable agreement with low-T neutron diffraction [30].

In type-II multiferroics, the observation of magnetoelectric phenomena is intricately linked to crystal and magnetic spin structures. In general, either spin-frustrated lattices or the symmetry-allowed magnetic space groups generates the finite electric polarization ME systems. However, neither the FiM structure nor its magnetic space group $P2_1/a$ of $Fe_2(MoO_4)_3$ supports the ME coupling, which agrees with the observation of the absence of P in the L-FiM spin structure below T_{N1} for $H = 0$ [30,39], which is consistent with the absence of second harmonic signal for the single crystals of $Fe_2(MoO_4)_3$ [29]. However, as displayed in Figs. 2 and 3, the concurrent emergence of T_{N2} and finite P strongly hints at a possible change of pre-existing L-FiM ordering and crystal symmetry under external H that might trigger modulated spin structures. Furthermore, the low P values perhaps eliminated the exchange-striction-induced ferroelectricity in $Fe_2(MoO_4)_3$ (Table S3 [32]). Indeed, the order of magnitude P matches several well-known noncollinear multiferroic systems, as shown in Table S3 [32] (see also Refs. [11–15,40,41] therein). This hints that the contribution of unconventional spin structures might explain P below T_{N2}. It is important to note that the low P is not a sufficient condition to rule out the exchange striction; indeed, other mechanisms such as $p-d$ hybridization and a combination of two or more

origins are also equally possible and need to be verified further.

Based on the spin-canting assumption, here we proposed one of the potential scenarios for the origin of spin-induced magnetoelectric coupling, where external H modulates the L-FiM ordering. Figures 5(a) and 5(b) represent a schematic variation of sublattice magnetization vs T for $H = 0$ T and 7 T. Figure 5(c) displays the variation of sublattice magnetization vectors in L-FiM. A magnetically induced conical magnetic ordering at one of the Fe sites is proposed for $H = 7$ T [shown in Fig. 5(d)]. This assignment is quite possible for $Fe_2(MoO_4)_3$ by comparing the Mössbauer analysis of the L-FiM $Li_3Fe_2(PO_4)_3$ system under H. The linear increase in the canting angle between the total H with the γ-ray directions suggests the canting of iron spins in the FeO_6 octahedra [42]. This canting was enhanced with increasing H, suggesting the formation of spin-spiral states. The linear variation in P vs H [Fig. 3(f)] strongly supports H-induced spin canting. Moreover, $Fe_2(MoO_4)_3$ is structurally complex and flexible, and the spin reorientation at the FeO_6 octahedra might occur via strong lattice coupling. From the bond length and bond angle analyses of the structural data (Table S2) [32], the average bond lengths of $\langle Fe2\text{-}O\rangle$ and $\langle Fe3\text{-}O\rangle$ are slightly different from those of the other two Fe sites, suggesting that Fe ions endure slightly different crystal fields. In fact, this was supported by the Mössbauer spectrum. The thermal evaluation of the somewhat different hyperfine fields indicates minor variations in the local crystal fields of the Fe sites [27,29] that cause slight differences in exchange interactions and finite FiM components [29]. Further, competition between the local crystal field and the magnetic anisotropy with the external Zeeman field may trigger coherent FeO_6 octahedral distortions that might lead to noncentrosymmetric polar space group $P2_1$ and the emergence of electrical polarization under external H. This may result in unconventional conical spin structures at the Fe sites [43], indeed, resolving the conical spins that generate a superposition of the L-type and transverse conical spin components.

The electric P in the noncollinear spin systems originates from the spin current via the inverse Dzyaloshinskii-Moriya (DM) model (Katsura-Nagaosa-Balatsky model) [4]. The Fe^{3+} (d^5; orbital angular momentum $L = 0$) electronic state rules out the spin-orbit mechanism. Considering the flexibility of the crystal structure and lattice ε' anomaly at T_{N1} for $H = 0$ T, one can anticipate that spin-lattice coupling plays a dominant role in the observed exotic multiferroicity under H in $Fe_2(MoO_4)_3$. Furthermore, this analysis adequately agrees with the proposal that an external H might distort the crystal lattice via FeO_6 octahedra rotation, and concurrently spin-reorientation and electric P occurred [43]. Meanwhile, the theoretical and experimental validity of the inverse-DM mechanism in these complex supersuperexchange interaction pathways might provide a deeper understanding of the magnetoelectric coupling in $Fe_2(MoO_4)_3$.

Observing H-induced second magnetic ordering and its associated electric coupling makes $Fe_2(MoO_4)_3$ a peculiar multiferroic distinct from other well-established spin-flip-induced type-II multiferroic members, for example, in systems like $TbMnO_3$, $CoCr_2O_4$, and $MnWO_4$, where structural
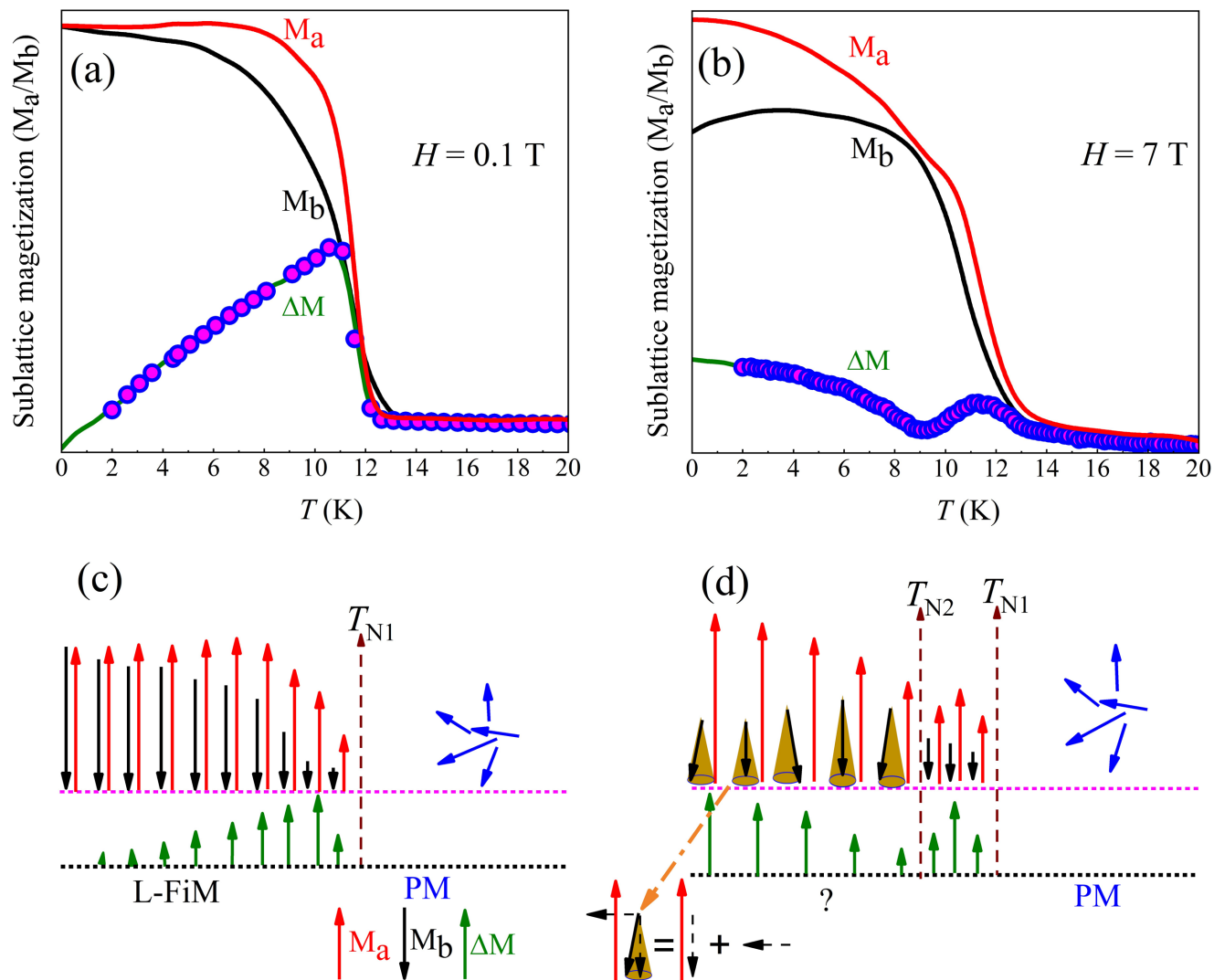
FIG. 5. (a) Schematic representation for the T variation of sublattice magnetizations compared with the experimental χ vs T curve for the L-FiM nature. (b) Subtle changes in the sublattice magnetizations of L-FiM under H where the multiferroic behavior has been observed. Simplified representation of the spin alignment of sublattice magnetization in. (c) L-FiM. (d) possible conical spin configuration at one of the Fe sites (for simplification, here we assumed two magnetic sublattices for four Fe^{3+} ions sites and each sublattice represents an FM coupled pair of Fe^{3+} ions). The red, black, and green lines and arrows illustrate the variation in the sublattice spins M_a, M_b, and $\Delta M = M_a - M_b$ respectively, whereas the blue arrows indicate the random spin alignment in the PM region.

changes usually drive the noncollinear magnetic configuration at zero fields. Then, the H-induced spin flop reorients the spin spiral plane between different crystallographic directions and leads to a giant electric P [13,14,44]. In contrast, the present system is very distinct such that H-induced entirely new magnetic and electrical orderings appear below L-FiM at T_{N1}. Although the proposed conical spin structure qualitatively explains the origin of multiferroic behavior, it further needs to be verified experimentally. At present, the actual spin structure below T_{N2} is unknown; different equally persuasive interpretations might, in principle, validate the observed exotic magnetoelectric nature. Further, possibilities of crystal structure change from $P2_1/a$ to polar $P2_1$ under magnetic field need to be investigated. Hence the origin of the magnetic-field-induced ferroelectricity is still an open question and needs to be resolved quantitatively. Therefore, growing single

crystal $Fe_2(MoO_4)_3$, analyzing its lattice and spin structure via neutron scattering, and probing the Fe electronic structure via optical spectrum below T_{N2} and under H are extremely demanded.

V. CONCLUSION

In summary, the magnetic and electric properties of $Fe_2(MoO_4)_3$ were investigated. (i) The L-FiM ordering at $T_{N1} \sim 12$ K was verified with $\chi(T)$ and $C_p(T)$ anomalies. (ii) Other than the anomaly that occurred at T_{N1}, an additional magnetic anomaly built up at lower temperature T_{N2} at increasing H shows an exotic magnetic ordering state. Thus, the H-induced conical magnetic state from the original L-FiM was proposed. (iii) The H-induced switchable ferroelectric polarization (P) was measured corresponding to the magnetic

state below T_{N2}. Thus, the type-II multiferroic behavior was established by the H-T phase diagram. (iv) In contrast to the commonly observed H-induced spin flip and P with a certain critical field (H_c) at T_{N1}, observed H-dependent T_{N2} and ME coupling was exotic. (v) The results open new thoughts for novel multiferroic mechanisms besides existing ones; therefore, more theoretical, and experimental works are needed for further exploration.

[1] W. Eerenstein, N. D. Mathur, and J. F. Scott, Nature **442**, 759 (2006).

[2] N. A. Hill, J. Phys. Chem. B **104**, 6694 (2000).

[3] S.-W. Cheong and M. Mostovoy, Nat. Mater. **6**, 13 (2007).

[4] Y. Tokura and S. Seki, Adv. Mater. **22**, 1554 (2010).

[5] Y. Tokura, S. Seki, and N. Nagaosa, Rep. Prog. Phys. **77**, 076501 (2014).

[6] M. Fiebig, T. Lottermoser, D. Meier, and M. Trassin, Nat. Rev. Mater. **1**, 16046 (2016).

[7] C.-W. Nan and J.-M. Liu, Natl. Sci. Rev. **6**, 620 (2019).

[8] S. Dong, H. Xiang, and E. Dagotto, Natl. Sci. Rev. **6**, 629 (2019).

[9] P. N. R. Sankar, S. Mishra, and A. Sundaresan, APL Mater. **8**, 040906 (2020).

[10] H. Katsura, N. Nagaosa, and A. V. Balatsky, Phys. Rev. Lett. **95**, 057205 (2005).

[11] Y. S. Oh, S. Artyukhin, J. J. Yang, V. Zapf, J. W. Kim, D. Vanderbilt, and S.-W. Cheong, Nat. Commun. **5**, 3201 (2014).

[12] Y. Wang, G. L. Pascut, B. Gao, T. A. Tyson, K. Haule, V. Kiryukhin, and S.-W. Cheong, Sci. Rep. **5**, 12268 (2015).

[13] T. Kimura, T. Goto, H. Shintani, K. Ishizaka, T. Arima, and Y. Tokura, Nature (London) **426**, 55 (2003).

[14] Y. Yamasaki, S. Miyasaka, Y. Kaneko, J. P. He, T. Arima, and Y. Tokura, Phys. Rev. Lett. **96**, 207204 (2006).

[15] Y. J. Choi, H. T. Yi, S. Lee, Q. Huang, V. Kiryukhin, and S. W. Cheong, Phys. Rev. Lett. **100**, 047601 (2008).

[16] S. Seki, X. Z. Yu, S. Ishiwata, and Y. Tokura, Science **336**, 198 (2012).

[17] H. C. Wu, K. D. Chandrasekhar, J. K. Yuan, J. R. Huang, J. Y. Lin, H. Berger, and H. D. Yang, Phys. Rev. B **95**, 125121 (2017).

[18] H. Liu, W. Sun, Z. Zhang, L. N. Lovings, and C. Lind, Solids **2**, 87 (2021).

[19] A. W. Sleight and L. H. Brixner, J. Solid State Chem. **7**, 172 (1973).

[20] L. E. Cross, A. Fouskova, and S. E. Cummins, Phys. Rev. Lett. **21**, 812 (1968).

[21] J. D. Axe, B. Dorner, and G. Shirane, Phys. Rev. Lett. **26**, 519 (1971).

[22] I.-E. Nylund, M. Tsoutsouva, T. Grande, and D. Meier, Phys. Rev. Mater. **6**, 034402 (2022).

[23] B. K. Ponomarev, S. A. Ivanov, B. S. Red'kin, and V. N. Kurlov, Physica B **177**, 327 (1992).

[24] H.-Y. Chen, Mater. Res. Bull. **14**, 1583 (1979).

[25] P. D. Battle, A. K. Cheetham, W. T. A. Harrison, N. J. Pollard, and J. Faber Jr., J. Solid State Chem. **58**, 221 (1985).

[26] M. H. Rapposch, J. B. Anderson, and E. Kostiner, Inorg. Chem. **19**, 3531 (1980).

[27] P. D. Battle, A. K. Cheetham, G. J. Long, and G. Longworth, Inorg. Chem. **21**, 4223 (1982).

[28] G. J. Long, in *Chemical Mössbauer Spectroscopy*, edited by R. H. Herber (Springer, Boston, MA, 1984), pp. 95–111.

[29] Z. Jirak, R. Salmon, L. Fournes, F. Menil, and P. Hagenmuller, Inorg. Chem. **21**, 4218 (1982).

[30] H. Ehrenberg, K. G. Bramnik, E. Muessig, T. Buhrmester, H. Weitzel, and C. Ritter, J. Magn. Magn. Mater. **261**, 353 (2003).

[31] W. Song, B. Yuan, X. Liu, Z. Li, J. Wang, and E. Liang, J. Mater. Res. **29**, 849 (2014).

[32] See Supplemental Material at http://link.aps.org/supplemental/10.1103/PhysRevMaterials.6.094412 for the SXRD refined structural details, lattice parameters, and average Fe-O bond lengths for all four FeO_6 octahedra, SEM micrograph, low field, and high field magnetization data on sample, along with a comparison of polarization mechanisms for known multiferroic magnets.

[33] T. Katsufuji, S. Mori, M. Masaki, Y. Moritomo, N. Yamamoto, and H. Takagi, Phys. Rev. B **64**, 104419 (2001).

[34] D. C. Kakarla, H. C. Wu, D. J. Hsieh, P. J. Sun, G. J. Dai, J. Y. Lin, J. L. Her, Y. H. Matsuda, L. Z. Deng, M. Gooch, C. W. Chu, and H. D. Yang, Phys. Rev. B **99**, 195129 (2019).

[35] A. Tiwari, D. C. Kakarla, G. Macam, C. H. Hsu, F. C. Chuang, H. C. Wu, T. W. Kuo, A. Pal, H. Chou, D. P. Gulo, H. L. Liu, Y. C. Chuang, Y. C. Lai, C. A. Lee, M. M. C. Chou, and H. D. Yang, Phys. Rev. Mater. **6**, 044409 (2022).

[36] A. Iyama and T. Kimura, Phys. Rev. B **87**, 180408(R) (2013).

[37] Y. Fang, Y. Q. Song, W. P. Zhou, R. Zhao, R. J. Tang, H. Yang, L. Y. Lv, S. G. Yang, D. H. Wang, and Y. W. Du, Sci. Rep. **4**, 3860 (2014).

[38] N. D. Khanh, N. Abe, H. Sagayama, A. Nakao, T. Hanashima, R. Kiyanagi, Y. Tokunaga, and T. Arima, Phys. Rev. B **93**, 075117 (2016).

[39] S. V. Gallego, J. Etxebarria, L. Elcoro, E. S. Tasci, and J. M. Perez-Mato, Acta Crystallogr., Sect. A **75**, 438 (2019).

[40] B. Kundys, C. Simon, and C. Martin, Phys. Rev. B **77**, 172402 (2008).

[41] T. Kimura, Y. Sekio, H. Nakamura, T. Siegrist, and A. P. Ramirez, Nat. Mater. **7**, 291 (2008).

[42] H. S. Kim and C. S. Kim, J. Appl. Phys. **115**, 17E126 (2014).

[43] J. M. Rondinelli and C. J. Fennie, Adv. Mater. **24**, 1961 (2012).

[44] O. Heyer, N. Hollmann, I. Klassen, S. Jodlauk, L. Bohatý, P. Becker, J. A. Mydosh, T. Lorenz, and D. Khomskii, J. Phys.: Condens. Matter **18**, L471 (2006).